Geophysical Journal International

Geophys. J. Int. (2012) doi: 10.1111/j.1365-246X.2012.05676.x

Numerical simulation of seismic wave propagation produced by earthquake by using a particle method

Junichi Takekawa,[1] Raul Madariaga,[2] Hitoshi Mikada[3] and Tada-nori Goto[3]

[1] *Civil & Earth Resources Engineering, Kyoto University,* C1-1-111, *Kyotodaigaku-Katsura, Nishikyoku, Kyoto* 615-8540, *Japan.*
E-mail: takekawa@tansa.kumst.kyoto-u.ac.jp
[2] *Ecole Normale Superieure, Paris, France*
[3] *Kyoto University, Kyoto, Japan*

Accepted 2012 September 11. Received 2012 August 31; in original form 2011 November 10

SUMMARY

We propose a forward wavefield simulation based on a particle continuum model to simulate seismic waves travelling through a complex subsurface structure with arbitrary topography. The inclusion of arbitrary topography in the numerical simulation is a key issue not only for scientific interests but also for disaster prediction and mitigation purposes. In this study, a Hamiltonian particle method (HPM) is employed. It is easy to introduce traction-free boundary conditions in HPM and to refine the particle density in space. Any model with complex geometry and velocity structure can be simulated by HPM because the connectivity between particles is easily calculated based on their relative positions and the free surfaces are automatically introduced. In addition, the spatial resolution of the simulation could be refined in a simple manner even in a relatively complex velocity structure with arbitrary surface topography. For these reasons, the present method possesses great potential for the simulation of strong ground motions.

In this paper, we first investigate the dispersion property of HPM through a plane wave analysis. Next, we simulate surface wave propagation in an elastic half space, and compare the numerical results with analytical solutions. HPM is more dispersive than FDM, however, our local refinement technique shows accuracy improvements in a simple and effective manner. Next, we introduce an earthquake double-couple source in HPM and compare a simulated seismic waveform obtained with HPM with that computed with FDM to demonstrate the performance of the method. Furthermore, we simulate the surface wave propagation in a model with a surface of arbitrary topographical shape and compare with results computed with FEM. In each simulation, HPM shows good agreement with the reference solutions. Finally, we discuss the calculation costs of HPM including its accuracy.

Key words: Numerical solutions; Numerical approximations and analysis; Earthquake ground motions; Computational seismology.

1 INTRODUCTION

The development of numerical schemes is of great importance in seismology to provide quantitative information for earthquake disaster prevention and mitigation, such as the simulation of earthquake generation, the estimation of ground shaking, etc. The most popular and widely used methods are those using the finite difference methods (FDM) with staggered grids (Madariaga 1976; Virieux 1986; Levander 1988; Graves 1996). Finite element methods (FEM) and spectral element methods (SEM), which are special kinds of FEM, have been also used to simulate seismic wave propagation (Komatitsch & Tromp 1999; Koketsu *et al.* 2004). These methods have advantages over FDM in the treatment of traction-free boundary conditions at the outer boundary of a medium. Furthermore, arbitrary mesh refinement adapted to the internal and external boundaries of the medium is possible even when the velocity structure of the model is complex. Mercerat *et al.* (2006) conducted numerical simulations of elastic wave propagation in a model with arbitrary topography of the free surface and internal material interfaces like a basin structure using SEM with a triangular mesh. Their results successfully reproduced a strong Rayleigh wave, a direct *P* wave, converted waves and so on. Koketsu *et al.* (2004) calculated seismograms in models with sedimentary basins and mountain structure using FEM with a voxel technique. They showed the effect of the sedimentary basin and mountain structure on ground velocity distributions using a refinement technique of spatial resolution.

Particle-based methods like the distinct element method (DEM; Cundall & Strack 1979) have been applied to the simulation of seismic wave propagation as an alternative to traditional continuum-based simulators (Toomey & Bean 2000). Elastic lattice methods (ELM) have also been applied to simulate seismic wave propagation, and the accuracy and dispersion analysis was conducted (Del Valle-Garcia & Sanchez-Sesma 2003; O'Brien & Bean 2004; O'Brien *et al.* 2009). More recently, Mariotti (2007) applied their Mka3D code to elasticity adapting their method based on the use of the microbeams between particles. The formulation can give a micro–macro relation for not only regular but also irregular lattices, and can treat full domain of Poisson's ratios and Young modulus. In Mariotti (2007), Voronoi diagrams were used to identify neighbouring particles which interacted with each other. Chikazawa *et al.* (2001) developed a particle scheme named moving particle semi-implicit (MPS) method for elastic and visco-plastic structures. Their scheme is also a mesh-less methods, and can simulate failure phenomena and fluid-structure interactions easily. If we use regular lattices of particles, the MPS method needs only the distances between particles to make connectivity between particles.

In this study, a Hamiltonian particle method (HPM) is applied to simulate seismic wave propagation. In HPM, the identification of neighbouring particles is based only on the distances between each particle like in Chikazawa *et al.* (2001). Finally, particle motion equation for each particle is derived such as DEM, ELM and MPS. In MPS and HPM, interaction between each pair of particles is weighted based on distance of the two particles, although the concept of the derivation of particle motion equation is different. The particle motions are formulated in the Hamiltonian framework and the deformation gradient tensor is approximated only at the particles. HPM was initially developed to calculate incompressible fluid flow with a free surface (Suzuki *et al.* 2007). Recently, solid deformation problems were also solved by HPM (Suzuki & Koshizuka 2008; Kondo *et al.* 2010).

In this study, we focus our attention on the strong ground motion produced by earthquakes. First we investigate the dispersion properties of HPM through a plane wave analysis. We, next, simulate surface wave propagation in an elastic half space and the scheme is compared with the analytical solution for Lamb's problem, and we apply a local refinement technique to improve its accuracy in a simple and effective manner. Next, we introduce earthquake double–couple sources in HPM and compare the result obtained by HPM with that from FDM. Surface wave propagation in a model, which has an arbitrary surface topography is calculated with HPM and is compared with the result from FEM. Finally, we compare the calculation costs of HPM with those of FDM.

2 METHOD

2.1 Theory

Cundall & Strack (1979) developed a particle-based approach to model rock mechanics problems called DEM. In DEM, particles are connected by virtual springs and interact with each other through both normal and shear forces at contact points. In HPM, on the other hand, we calculate the particle motion based on the deformation gradient tensor estimated at each particle position.

In HPM, each particle interacts with the neighbouring particles, which are at a certain distance from it (Fig. 1). This domain, which defines the interaction area is called the influence domain. The influence domain defines a circular area or a spherical volume in 2-D or 3-D problems, respectively. The number of neighbouring particles is controlled by the radius of the influence domain. The effect of the radius on seismogram will be discussed in the following chapter.

We consider a weighting function $w(r)$ between particles to weight their interactions as follows.

$$w(r) = r_e/r - 1 \,(r \leq r_e) \quad \text{or} \quad 0 \,(r > r_e), \tag{1}$$

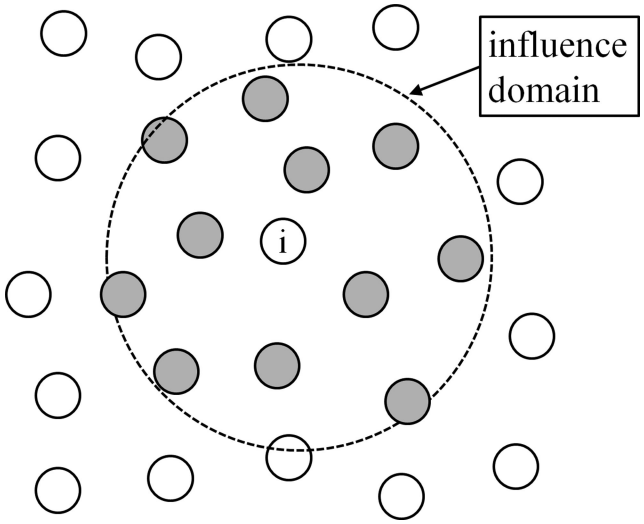

Figure 1. The particles in the influence domain. In this figure, the shaded particles are the selected ones.

where r is the distance between particles and r_e is the averaged radius of the influence domain. The weighting value at the considered particle is infinite, and becomes zero outside the influence domain. r_e is calculated as follows,

$$r_e = \left(r_{ei} + r_{ej}\right)/2, \tag{2}$$

where r_{ei} and r_{ej} are the influence domains of particle i and j. The influence domain of each particle depends on their radius.

$$r_{ei} = \alpha d_i \tag{3}$$

d_i is the radius of particle i, α is the coefficient which controls the number of neighbouring particles.

In HPM, the deformation gradients at the position of particle i is evaluated by minimizing the error function e_i,

$$e_i = \sum_j \left|\mathbf{F}_i \mathbf{r}_{ij}^0 - \mathbf{r}_{ij}\right|^2 w_{ij}^0, \tag{4}$$

where $\mathbf{F}_i$ is the deformation gradient tensor at the position of particle i, $\mathbf{r}_{ij}^0$ and $\mathbf{r}_{ij}$ are the initial and current position of particle j relative to particle i, respectively, w_{ij}^0 is the weighting function between particle i and j calculated by eq. (1). Minimizing the deformation gradient tensor eq. (4), we get

$$\begin{aligned} \partial e_i/\partial \mathbf{F}_i &= 2\sum_j w_{ij}^0 \left(\mathbf{r}_{ij} - \mathbf{F}_i \mathbf{r}_{ij}^0\right) \otimes \left(-\mathbf{r}_{ij}^0\right) \\ &= -2\sum_j w_{ij}^0 \mathbf{r}_{ij} \otimes \mathbf{r}_{ij}^0 + 2\mathbf{F}_i \sum_j w_{ij}^0 \mathbf{r}_{ij}^0 \otimes \mathbf{r}_{ij}^0 \\ &= 0 \end{aligned} \tag{5}$$

$$\mathbf{F}_i = \sum_j \mathbf{r}_{ij} \otimes \mathbf{r}_{ij}^0 w_{ij}^0 \mathbf{A}_i^{-1} \tag{6}$$

$$\mathbf{A}_i = \sum_j \mathbf{r}_{ij}^0 \otimes \mathbf{r}_{ij}^0 w_{ij}^0, \tag{7}$$

where a symbol $\otimes$ means tensor product. We use eq. (6) anywhere in the analysis model. If the calculation model includes a discontinuous surface (e.g. liquid–solid interface), the approximation of eq. (6) may include the error due to this assumption.

The total elastic strain energy is written using strain $\mathbf{E}$ and stress $\mathbf{S}$, which can be calculated from the deformation gradient tensor.

$$V = \sum_i \left(\mathbf{E}_i : \mathbf{S}_i \Delta B_i\right)/2 \tag{8}$$

$$\mathbf{E} = \left(\mathbf{F}^{\mathrm{T}}\mathbf{F} - \mathbf{I}\right)/2 \tag{9}$$

$$\mathbf{S} = 2\mu\mathbf{E} + \lambda \mathrm{tr}\left(\mathbf{E}\right)\mathbf{I}, \tag{10}$$

where V is the total elastic strain energy, ΔB_i is the volume of particle i, λ and μ are Lame's coefficient. Eq. (10) indicates that we adopt the Saint Venant-Kirchhoff (linear elastic) model for a constitutive law. When a regular particle arrangement is used, it is simple to calculate the volume occupied by each particle. When irregular lattices, however, are used as in the following chapter, the volumes of divided particles need to be allocated based on division number, and those of displaced particles are maintained. The medium coefficients are defined on each particle.

The total kinetic energy is defined as follows,

$$K = \sum_i \left(m_i \left|\mathbf{v}_i\right|^2\right)/2, \tag{11}$$

where $\mathbf{v}_i$ is the velocity of particle i, and m_i is its mass. The mass is calculated as follows,

$$m_i = \rho_i \Delta B_i, \tag{12}$$

where ρ_i is the density of particle i. The total energy of the system H is the Hamiltonian $H = V + K$. Then we can calculate the equation of motion of each particle using Hamilton's equation;

$$\begin{aligned} \rho_i \Delta B_i \partial \mathbf{v}_i/\partial t &= -\partial H/\partial \mathbf{x}_i \\ &= \sum_j \left(\mathbf{F}_i \mathbf{S}_i \mathbf{A}_i^{-1} \mathbf{r}_{ij}^0 \Delta B_i + \mathbf{F}_j \mathbf{S}_j \mathbf{A}_j^{-1} \mathbf{r}_{ij}^0 \Delta B_j\right) w_{ij}^0 \cdot \end{aligned} \tag{13}$$

We compute the behaviour of the elastic body using the following time stepping algorithm.

$$\mathbf{x}^{t+\Delta t} = \mathbf{x}^t + \Delta t \cdot \mathbf{v}^t \tag{14}$$

$$\mathbf{v}^{t+\Delta t} = \mathbf{v}^t + \Delta t \cdot \left(\partial \mathbf{v}/\partial t\right)^{t+\Delta t} \tag{15}$$

This symplectic scheme is effective to conserve total energy in spite of its simplicity.

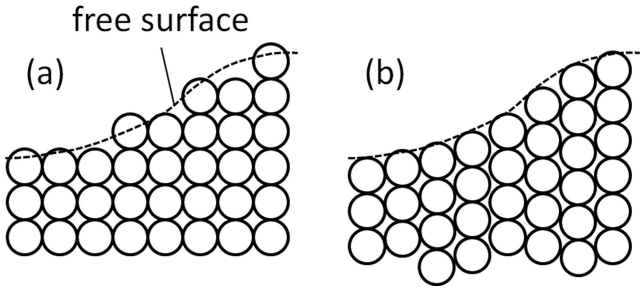

Figure 2. The arrangement of particles in HPM.

2.2 Particle arrangement

In HPM, we can use an arbitrary arrangement of particles. To model non-flat free surface using HPM, several strategies can be used to define the topography as shown in Fig. 2. In Fig. 2(a), particles whose positions are above the free surface are simply removed from regular lattice arrangement. This simple method is unfortunately not very accurate. In Fig. 2(b), particles are displaced from their original positions to fit the topology of the surface. Since the interaction model is constructed based only on the positions of particles in HPM, irregular arrangement of particles is accepted without inhomogeneous and anisotropy. This arrangement can model more accurate topography than that of Fig. 2(a), the volume is also calculated easily like in Fig. 2(a). In the following chapters, we use the arrangement of Fig. 2(b) to model non-flat free surfaces.

3 DISPERSION ANALYSIS

Since wave speed is a function of wavelength in numerical methods (e.g. Mullen & Belytschko 1982; Marfurt 1984), we perform a plane wave analysis to investigate the dispersion properties of HPM. In this section, we consider only a 2-D regular lattice alignment of particles and *P*-wave propagating along the *x*-direction. Our model has a *P*-wave velocity of $V_p = 4000\ \mathrm{m\ s^{-1}}$, and a mass density of $\rho = 2200\ \mathrm{kg\,m^{-3}}$. Particle spacing of regular lattice is 10 m, the coefficient of the influence domain in eq. (3) is set to 1.9.

We consider a plane wave of the form $\mathbf{u} = \mathrm{u}_0 \mathrm{e}^{-\mathrm{i}\omega t + \mathrm{i}kx}$ propagating along the *x*-direction with wavenumber k and frequency ω. u_0 is the amplitude of the plane wave. Inserting it into eq. (6) yields

$$\mathbf{F}_i = \begin{pmatrix} 1 + \frac{1}{2\Delta x}\left(\mathrm{e}^{\mathrm{i}k\Delta x} - \mathrm{e}^{-\mathrm{i}k\Delta x}\right) u_0 \mathrm{e}^{-\mathrm{i}\omega t + \mathrm{i}kx} & 0 \\ 0 & 1 \end{pmatrix}, \tag{16}$$

where Δx is the particle spacing. Inserting eq. (16) into eqs (9) and (10), the stress tensor of particle i could be calculated.

$$S = \begin{pmatrix} (\lambda + 2\mu)\frac{1}{2}\left\{(1+U)^2 - 1\right\} & 0 \\ 0 & \lambda\frac{1}{2}\left\{(1+U)^2 - 1\right\} \end{pmatrix}, \tag{17}$$

where;

$$U = \frac{1}{2\Delta x}\left(\mathrm{e}^{\mathrm{i}k\Delta x} - \mathrm{e}^{-\mathrm{i}k\Delta x}\right) u_0 \mathrm{e}^{-\mathrm{i}\omega t + \mathrm{i}kx}. \tag{18}$$

The deformation gradient and the stress tensors of the surrounding particles can be calculated in the same manner. Inserting them into eq. (13) yields

$$\begin{aligned} -\rho\Delta B\omega^2 u_0 \mathrm{e}^{-\mathrm{i}\omega t + \mathrm{i}kx} = {} & \frac{1}{4\Delta x^2}(\lambda + 2\mu)\left(\mathrm{e}^{2ik\Delta x} + \mathrm{e}^{-2ik\Delta x} - 2\right)\Delta B u_0 \mathrm{e}^{-i\omega t + ikx} \\ & + \frac{3}{16\Delta x^3}(\lambda + 2\mu)\left\{2\left(\mathrm{e}^{-2ik\Delta x} - \mathrm{e}^{2ik\Delta x}\right) + \left(\mathrm{e}^{4ik\Delta x} - \mathrm{e}^{-4ik\Delta x}\right)\right\}\Delta B u_0^2 \mathrm{e}^{2(-i\omega t + ikx)} \\ & + \frac{1}{32\Delta x^4}(\lambda + 2\mu)\left\{\left(\mathrm{e}^{6ik\Delta x} + \mathrm{e}^{-6ik\Delta x}\right) - 3\left(\mathrm{e}^{4ik\Delta x} + \mathrm{e}^{-4ik\Delta x}\right) + 3\left(\mathrm{e}^{2ik\Delta x} + \mathrm{e}^{-2ik\Delta x}\right) - 2\right\}\Delta B u_0^3 \mathrm{e}^{3(-i\omega t + ikx)}. \end{aligned} \tag{19}$$

The second and third terms in the right-hand side of eq. (19) are higher-orders. Dividing eq. (19) by $u_0 e^{-i\omega t + ikx}$, we obtain the following expression.

$$\begin{aligned} -\rho\Delta B\omega^2 = {} & \frac{1}{4}\left(\frac{1}{\Delta x^2}\right)(\lambda + 2\mu)\left(\mathrm{e}^{2ik\Delta x} + \mathrm{e}^{-2ik\Delta x} - 2\right)\Delta B \\ & + \frac{3}{16}\left(\frac{u_0}{\Delta x^3}\right)(\lambda + 2\mu)\left\{2\left(\mathrm{e}^{-2ik\Delta x} - \mathrm{e}^{2ik\Delta x}\right) + \left(\mathrm{e}^{4ik\Delta x} - \mathrm{e}^{-4ik\Delta x}\right)\right\}\Delta B \mathrm{e}^{-i\omega t + ikx} \\ & + \frac{1}{32}\left(\frac{u_0^2}{\Delta x^4}\right)(\lambda + 2\mu)\left\{\left(\mathrm{e}^{6ik\Delta x} + \mathrm{e}^{-6ik\Delta x}\right) - 3\left(\mathrm{e}^{4ik\Delta x} + \mathrm{e}^{-4ik\Delta x}\right) + 3\left(\mathrm{e}^{2ik\Delta x} + \mathrm{e}^{-2ik\Delta x}\right) - 2\right\}\Delta B \mathrm{e}^{2(-i\omega t + ikx)}. \end{aligned} \tag{20}$$

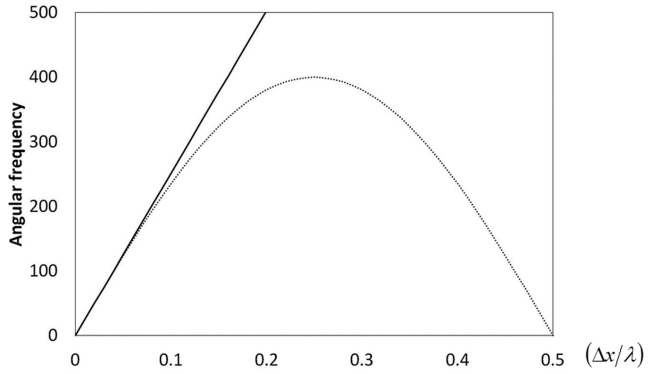

Figure 3. Dispersion curve of HPM. Solid and dotted curves are for the theoretical non-dispersive and numerical cases, respectively.

Here, we assume that the particle spacing Δx is much larger than the amplitude of the incident wave. In this case, the relation between the wavenumber and the frequency becomes very simple form as follows.

$$\omega \cong \sqrt{\frac{(\lambda + 2\mu)}{\rho \Delta x^2}} \sin(k\Delta x) \tag{21}$$

In the following models, the above assumption between the particle spacing and the amplitude of the incident wave is kept. Fig. 3 shows the dispersion relation of eq. (21).

4 SEISMIC WAVE PROPAGATION

4.1 Surface wave propagation

We test HPM using the classic Lamb problem as shown in Fig. 4. In this section, we use uniform arrangement of particles to represent a flat surface. The particle spacing is set to 10 m, and time spacing is 1 ms. The total calculation time is 3.5 s. Eight receivers are set at 0.1 km depth at equal distances from compressional source from 1.0 to 3.8 km. The time history of the source is the first derivative of a Gaussian with a central frequency of 4 Hz.

We studied two models A and B of an elastic homogeneous and isotropic medium. Model A has a *P*-wave velocity of $V_p = 2611\,\mathrm{m\,s^{-1}}$, an *S*-wave velocity of $V_S = 1846\,\mathrm{m\,s^{-1}}$, and a mass density of $\rho = 2200\,\mathrm{kg\,m^{-3}}$. On the other hand, model B has a *P*-wave velocity of $V_p = 4522\,\mathrm{m\,s^{-1}}$, an *S*-wave velocity of $V_S = 1846\,\mathrm{m\,s^{-1}}$, and a mass density of $\rho = 2200\,\mathrm{kg\,m^{-3}}$. Models A and B have Poisson ratios of 0.0 and 0.4, respectively. In our model, the higher frequency of the Gaussian is about 11 Hz, so that about 15 particles will be needed for the minimum wavelength for particles of 10 m.

As described earlier, the solution of HPM depends on the radius of the influence domain. We study the effect of the influence domain using three different values of α: 1.9, 2.1 and 2.3. The number of particles inside each influence domain is 8, 12 and 20 for these values of α.

We use analytical solution of Lamb's problem as a reference to compare analytical and numerical solutions, and we compute the misfit by

$$\text{Misfit} = \sum_t \left(S^{\text{HPM}}(t) - S^{\text{REF}}(t)\right)^2 \Big/ \sum_t S^{\text{REF}}(t)^2, \tag{22}$$

where $S^{\text{HPM}}(t)$ is the HPM seismogram and $S^{\text{REF}}(t)$ is the referential seismogram. The misfit is calculated over the whole seismogram.

Fig. 5 shows the displacement seismograms at receivers located in the horizontal and vertical directions for model A and B with different influence domains. Solid and dashed lines are analytical and numerical seismograms, respectively. The dotted line represents the difference

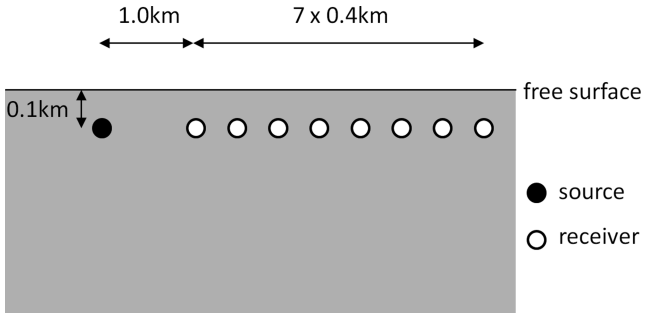

Figure 4. Geometry of the source and receivers in an elastic half-space.

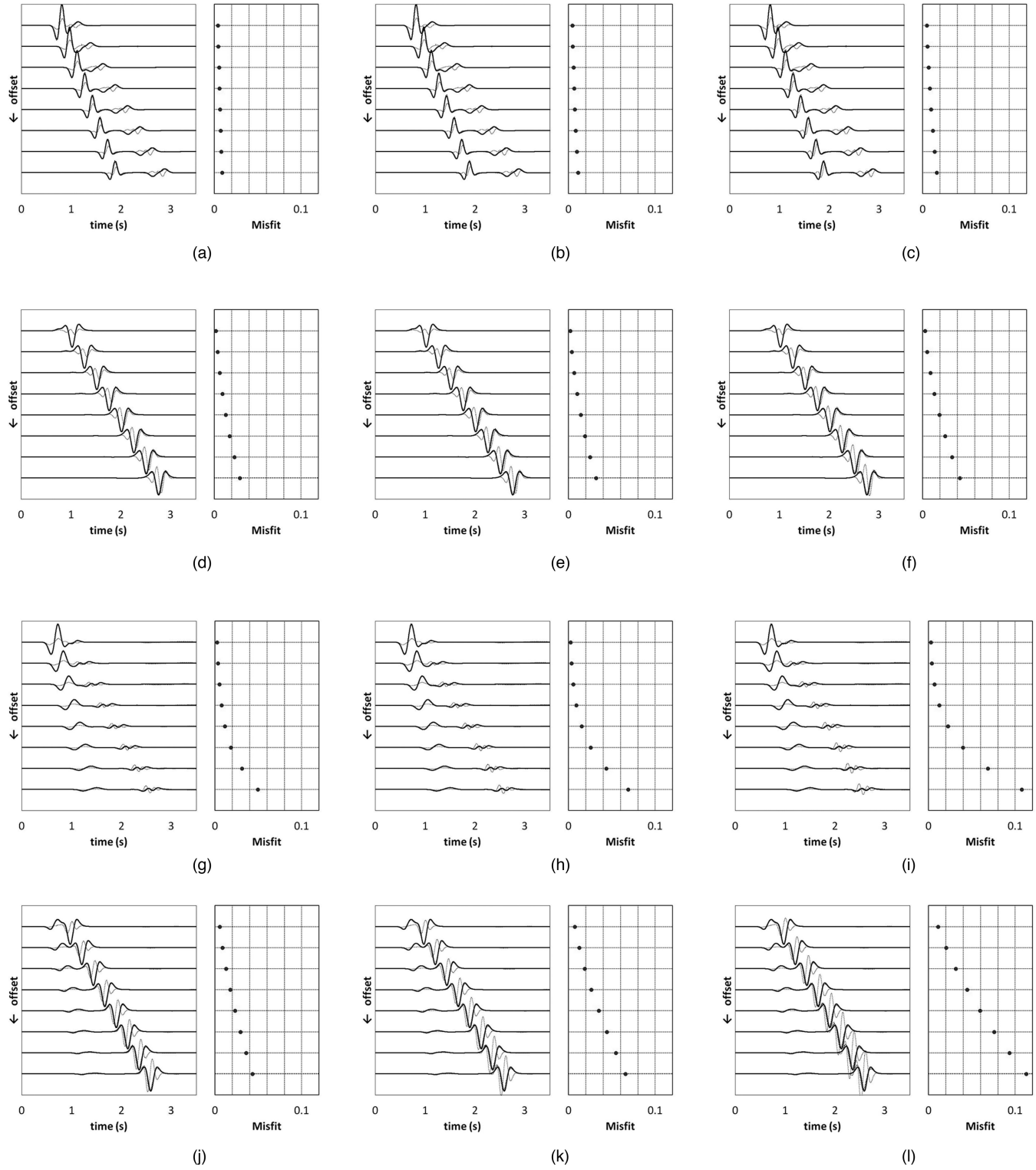

Figure 5. (a) Horizontal displacement at the receivers for model A with the coefficient of 1.9. (b) Horizontal displacement at the receivers for model A with the coefficient of 2.1. (c) Horizontal displacement at the receivers for model A with the coefficient of 2.3. (d) Vertical displacement at the receivers for model A with the coefficient of 1.9. (e) Vertical displacement at the receivers for model A with the coefficient of 2.1. (f) Vertical displacement at the receivers for model A with the coefficient of 2.3. (g) Horizontal displacement at the receivers for model B with the coefficient of 1.9. (h) Horizontal displacement at the receivers for model B with the coefficient of 2.1. (i) Horizontal displacement at the receivers for model B with the coefficient of 2.3. (j) Vertical displacement at the receivers for model B with the coefficient of 1.9. (k) Vertical displacement at the receivers for model B with the coefficient of 2.1. (l) Vertical displacement at the receivers for model B with the coefficient of 2.3.

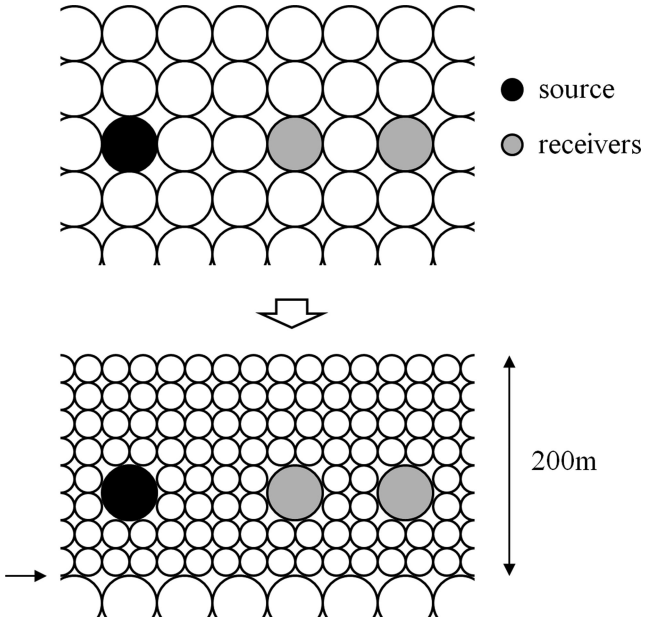

Figure 6. The local and arbitrary refinement of spatial resolution. The refinement is conducted just by dividing particles.

between the seismograms but the amplitude is amplified by a factor of 5. The amplitudes of all seismograms are normalized. For both models, the smaller radius of the influence domain produces smaller errors. This indicates that the influence domain with compact support is better than that with a broad one. The accuracy of HPM depends on the linearity of the deformation inside the influence domain because the deformation gradient tensor is approximated by eq. (6). This will cause larger misfits in larger influence domains. It is good that the smaller domain has better accuracy, because the calculation costs can be reduced. We will use the coefficient of 1.9 in the following sections.

We also conduct finite difference simulations with fourth-order staggered-grid the same configuration of Fig. 4. We use 10, 20, 25 and 50 m for the grid spacing Δx. For grid 10, 20 and 25 m, the results from FDM are good agreement with the analytical solutions. The misfits of FD simulations for 25 m are less than half of those from HPM in case of a grid of 10 m. For a grid of 50 m, dispersion becomes very large, and we observe a significant increase in the misfits. This shows that the HPM is more dispersive than FDM with forth-order staggered-grid if we use same grid or particle spacing.

We, next, apply a local refinement of the particle only near the ground surface as shown in Fig. 6. Refinement is conducted just by dividing one particle into four particles. At the interface between two particles indicated by an arrow in Fig. 6, special treatment as in FDM (Aoi & Fujiwara 1999) is not needed in HPM. So the refinement is implemented very easily. Source and receiver particles are not refined to keep the same relative positions between source, receivers and free surface. The irregular refinement shown in Fig. 6 is also easy to implement in HPM. Note that the time spacing should be changed depending on the minimum particle spacing for stable calculations. Again, the coefficient α in eq. (3) is set to 1.9.

Fig. 7 shows the seismograms of the displacement at the receivers in the horizontal and vertical direction for model A and B, and the misfits calculated by eq. (22). The local refinement of particles improves the accuracy. These results show that we can refine the spatial resolution using irregular grids and local refinement of the number of particles. This technique provides effective improvement of the accuracy in a simple and easy manner.

4.2 Introduction of a double–couple source in HPM

The earthquake double–couple source can be represented in HPM by a distribution of body-force couples centred at a certain particle location. Let the x' direction be defined as the direction along the plane of dislocation and let the y' and z' direction be directions perpendicular to x'.

The particle located at the source location is defined as particle 'i'. First, we have to decide to which particles body forces are to generate the moment M_0. Here, we use particles in the influence domain of particle 'i'. Next, we split the neighbouring particles in two parts along the plane of the shear fault (upper and lower parts) and calculate the length of the arm of each particle 'h_j'. The upper and lower particles are loaded by a body-forces directed in opposite directions and contribute to generate the required moment M_0. Here, the following strength of the body-force is added to each particle 'j'.

$$f_{x'j}(t) = h_j M_0(t)/H \text{ (upper part)} \tag{23}$$

$$f_{x'j}(t) = -h_j M_0(t)/H \text{ (lower part)} \tag{24}$$

$$H = \sum^{h_j^2}. \tag{25}$$

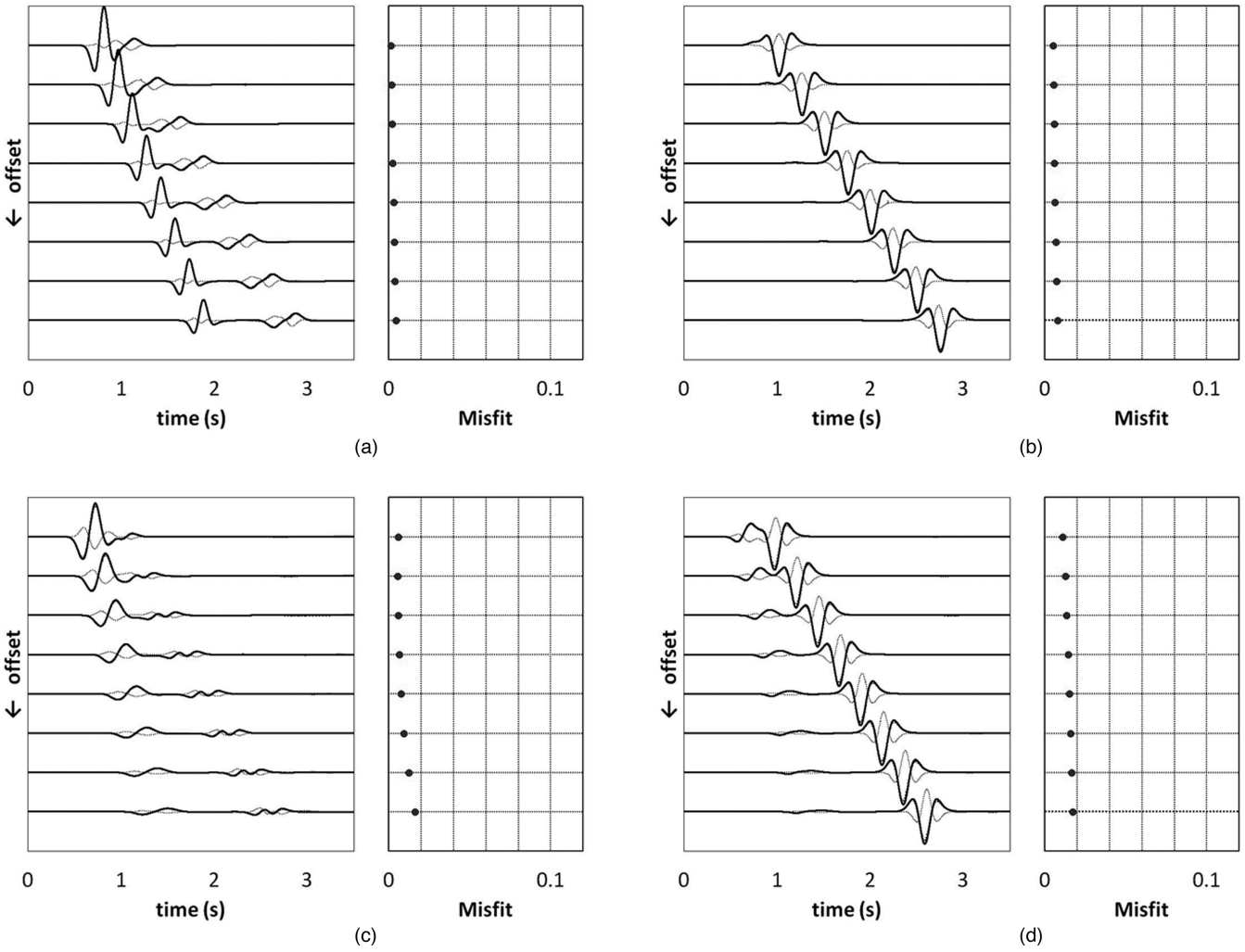

Figure 7. (a) Horizontal displacement at the receivers for model A with a coefficient of α 1.9 after the refinement. (b) Vertical displacement at the receivers for model A with a coefficient of α 1.9 after the refinement. (c) Horizontal displacement at the receivers for model B with a coefficient of α 1.9 after the refinement. (d) Vertical displacement at the receivers for model B with a coefficient of α 1.9 after the refinement.

The moment, which acts in the opposite direction, can be considered in a similar fashion. This concept can be expanded to 3-D problems easily though this paper covers only 2-D problems.

We calculate the seismic response for a fundamental point source to demonstrate the effectiveness of our source description in HPM by comparing with the results from FDM. Fig. 8(a) shows a test model for seismic wave propagation in a 2-D full-space. The model is discretized

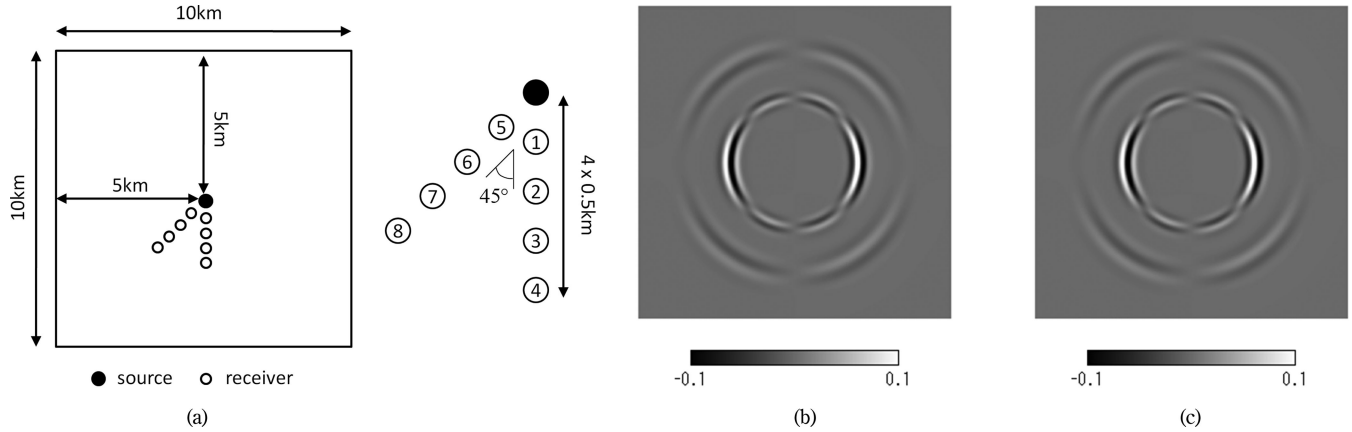

Figure 8. (a) Schematic model for the test of double–couple source description. (b) The snapshots of the velocity field in the vertical direction after 1.3 s calculated by HPM. (c) The snapshots of the velocity field in the vertical direction after 1.3 s calculated by FDM.

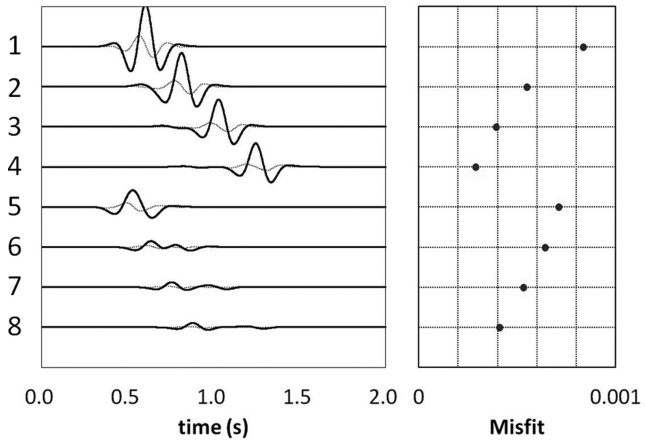

Figure 9. The seismogram of displacement in the horizontal direction.

by 1001×1001 particles and grids in HPM and FDM, respectively. The model is assumed to be a homogeneous medium and has a *P*-wave velocity of $V_p = 4000\,\mathrm{m\,s^{-1}}$, *S*-wave velocity of $V_S = 2310\,\mathrm{m\,s^{-1}}$, and mass density of $\rho = 2700\,\mathrm{kg\,m^{-3}}$. The particle distance Δx and time spacing Δt are 10 m and 1 ms, respectively. The coefficient of the radius of the influence domain is set to 1.9. The source time function is a Ricker wavelet with a central frequency of 4 Hz. The double couple source is located in centre of the model. The direction of shear dislocation is set to be horizontal, and the maximum displacement is 0.01 m. Eight receivers are located along a vertical and a diagonal line the numbering of each receiver is as shown in Fig. 8(a).

Figs 8(b) and (c) show the snapshots of the displacement velocity field in the vertical direction calculated with HPM and FDM after 1.3 s. The earthquake source description in FDM is based on that of Graves (1996). The results of both methods show the four-quadrant distribution of the displacement velocity field and the result from HPM is in good agreement with that from FDM. Fig. 9 shows the time histories of the displacement field at receiver points in the horizontal direction calculated by HPM and FDM. The differences between the two simulations amplified by a factor 10 and the misfit calculated by eq. (22) are also shown in the same figure. In the receivers close to the double–couple source (No.1 and 5), the misfits are larger than those observed at far receivers. This is caused by the difference in the definition of the source. However, the misfits are less than 0.1 per cent in each receiver. Since FDM is widely used and has been shown to reproduce seismic wavefield accurately, these results indicate that HPM can reproduce the seismic wavefield generated by a double–couple earthquake source with sufficient accuracy.

4.3 Arbitrary surface topography

It is very important for earthquake disaster prediction and mitigation to simulate the propagation of surface waves, which propagate at shallow depths and possess considerable energy. In HPM, the traction-free boundary condition can be implemented by ignoring the influence of the outer surrounding particles by assuming that the density of the surrounding continuum is very small compared to that of the interior continuum (Suzuki *et al.* 2007; Suzuki & Koshizuka 2008). Since the outer continuum is the air in the usual simulations of seismic ground motion, the traction-free boundary condition can be implemented easily. We use the alignment method shown in Fig. 2(b) as the particle arrangement strategy. In this paper, we deal with only two-dimensional problems; however this feature of HPM works well especially in 3-D analyses.

We conduct a numerical simulation of surface wave propagation on the model shown in Fig. 10, to test the effectiveness of HPM to simulate a free surface. The simulation based on FEM with four-node rectangular elements is used as a reference. The model has a *P*-wave velocity of $4000\,\mathrm{m\,s^{-1}}$, and an *S*-wave velocity of $2310\,\mathrm{m\,s^{-1}}$, and a mass density of $\rho = 2700\,\mathrm{kg\,m^{-3}}$. The particle distance Δx, time spacing Δt and the source time function are the same as that of Section 4.2. The receivers are located on the free surface.

Figs 10(b)–(e) show the snapshots of the results of seismic wave propagation after 2.0, 2.5, 3.0 and 3.5 s. It can be seen that the body waves and the surface wave run up the smooth slope. The waves are reproduced smoothly near the free surface. Fig. 11 shows the time histories of the displacement in the vertical direction at the receiver points. FE solutions, differences between HPM and FEM amplified by a factor 5, and the misfits calculated by eq. (22) are also shown in the figure. The seismograms simulated by HPM are in very good agreement with those from FEM. The misfit at the farthest receiver is less than 1 per cent.

4.4 Calculation costs

It is important to compare the calculation costs of HPM with those of other methods. In this section, we compare the calculation costs in terms of memory and computation time between HPM and FDM for the model of Section 4.2. The comparison with FEM can be analogized by the comparison between FEM and FDM in the literatures (e.g. Koketsu *et al.* 2004). The number of particles, time spacing, total time,

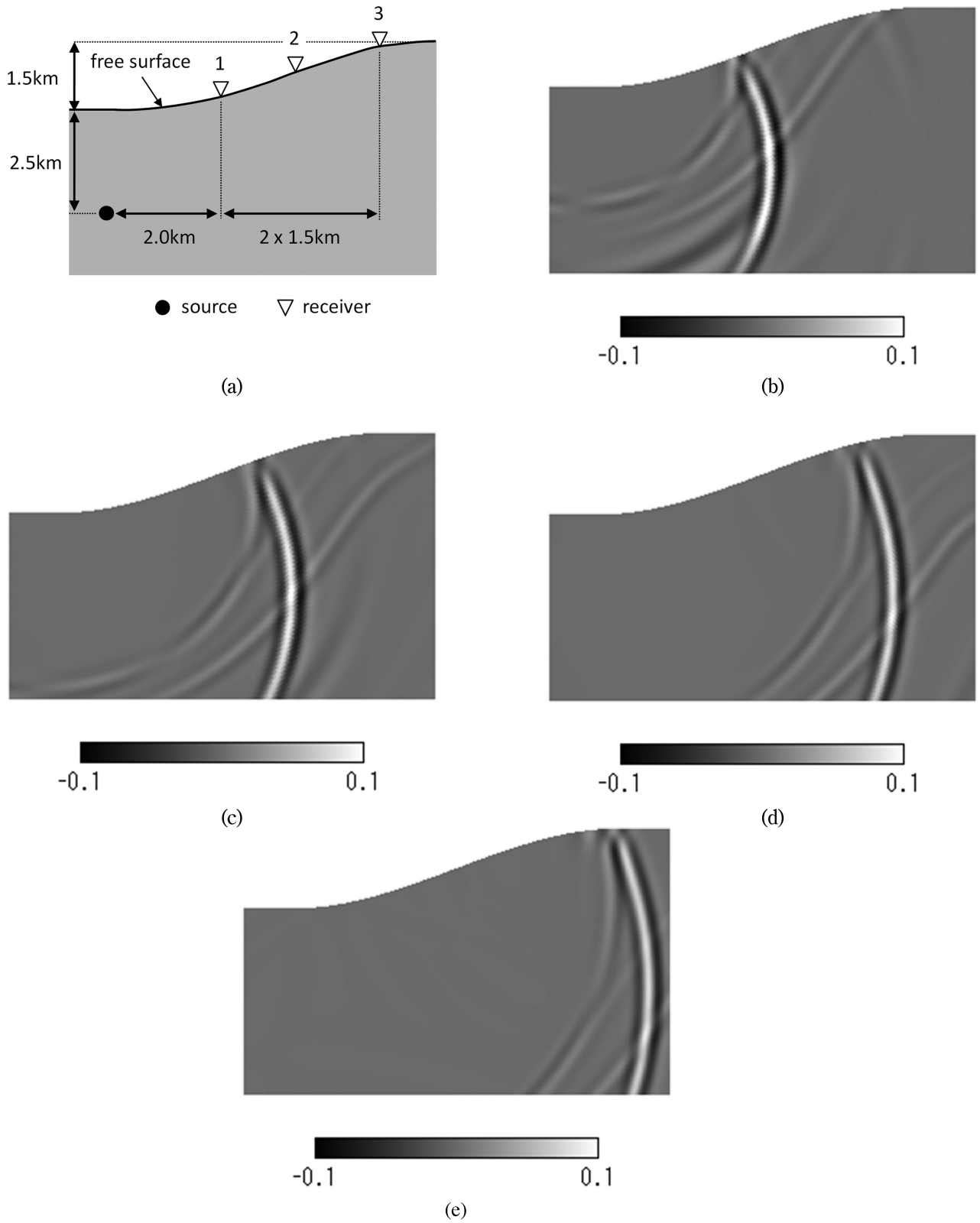

Figure 10. (a) Geometry of the numerical model with an arbitrary free surface. (b) The snapshots of the displacement velocity field in the vertical direction after 2.0 s. (c) The snapshots of the displacement velocity field in the vertical direction after 2.5 s. (d) The snapshots of the displacement velocity field in the vertical direction after 3.0 s. (e) The snapshots of the displacement velocity field in the vertical direction after 3.5 s.

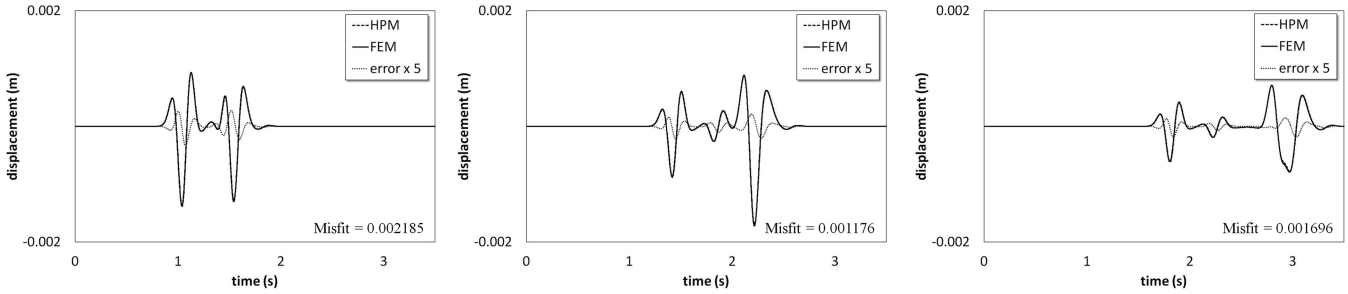

Figure 11. (a) The seismogram of displacement in the vertical direction at the receiver 1. (b) The seismogram of displacement in the vertical direction at the receiver 2. (c) The seismogram of displacement in the vertical direction at the receiver 3.

Table 1. The comparison between the calculation costs of HPM and those of FDM.

	Time (ms)	Memory (Byte)
HPM	2 282 458	533 442 560
FDM	726 630	131 432 448

particle spacing are the same as in Section 4.2. The calculation costs depend on the number of particles in the influence domain. As in the previous simulations, the coefficient of the influence domain is set to 1.9.

Table 1 shows the result of the comparison of calculation costs with FDM. The calculation time and computational memory of HPM are about triple and quadruple as much as those of FDM, respectively. Furthermore, the results in Section 4.1 showed that HPM is more dispersive than FDM. If we obtain same accuracy as FDM, HPM needs less than half the particle spacing. From these results, it appears that FDM has an advantage over HPM in the calculation costs because of the geometric regularity of the grids. In HPM, we need additional calculations and storage areas for the grid- or mesh-free calculations such as the weighting function between particles. Conversely, this enables us to operate irregular arrangement and refinement of particles. So, the data preparation time in pre-process will diminish using HPM. If we simulate seismic wave propagation in a simple model without topography and velocity contrasts, FDM will be more efficient due to its simpler calculations. However, if we need to consider topography like a mountain and velocity contrasts like in a sedimentary basin structure for the prediction of ground motion, HPM has a clear advantage over FDM. Though it is difficult to make an easy comparison, we consider that HPM can compete against other methods and has large potential.

5 CONCLUSIONS

In this study, we implemented HPM to simulate seismic wave propagation. We first investigated the dispersion properties of HPM through a plane wave analysis. We, next, conducted surface wave propagation simulations to test HPM by comparing with analytical solutions. The results show good agreement with the analytical ones and the irregular and local refinement of particles successfully improved the accuracy. Furthermore, we included an earthquake source in HPM as initial conditions and calculated the seismic response for a fundamental double couple point source. We compared the results from HPM with those from fourth-order staggered grid FDM. Results from our numerical simulations showed good agreement with those from FDM. Finally, we calculated the surface wave propagation at a free surface with arbitrary topography to demonstrate the advantage of HPM. Our simulation results showed accurate surface wave propagation on the complex ground surface.

The advantages of HPM are the simplicity and flexibility to create numerical models containing arbitrary topography shapes and the simplicity of its data structure. Furthermore, refinement of spatial resolution is possible in a simple manner because of the ability to use different particle sizes. These will provide us with easy and simple procedure to obtain desirable accuracy. Our results suggest that the method can be an alternative to existing numerical simulators of seismic wave propagation.

ACKNOWLEDGMENTS

This work was supported by the JSPS Institutional Program for Young Researcher Overseas Visits and by MEXT/JSPS KAKENHI Grant Number 24760361. We thank the editor Jean Virieux and two anonymous reviewers for their thoughtful comments and suggestions.

REFERENCES

Aoi, S. & Fujiwara, H., 1999. 3D finite-difference method using discontinuous grids, *Bull. seism. Soc. Am.,* **89,** 918–930.

Chikazawa, Y., Koshizuka, S. & Oka, Y., 2001. A particle method for elastic and visco-plastic structures and fluid-structure interactions, *Compt. Mech.,* **27,** 97–106.

Cundall, P.A. & Strack, O.D.L., 1979. A discrete numerical model for granular assemblies, *Geotechnique,* **29,** 47–65.

Del Valle-Garcia, R. & Sanchez-Sesma, F.J., 2003. Rayleigh waves modeling using an elastic lattice model, *Geophys. Res. Lett.,* **30,** 1866, doi:10.1029/2003GL017600.

Graves, R.W., 1996. Simulating seismic wave propagation in 3D elastic media using staggered-grid finite differences, *Bull. seism. Soc. Am.,* **86,** 1091–1106.

Koketsu, K., Fujiwara, H. & Ikegami, Y., 2004. Finite-element simulation of seismic ground motion with a voxel mesh, *Pure appl. Geophys.,* **161,** 2183–2198.

Komatitsch, D. & Tromp, J., 1999. Introduction to the spectral element method for three-dimensional seismic wave propagation, *Geophys. J. Int.,* **139,** 806–822.

Kondo, M., Suzuki, Y. & Koshizuka, S., 2010. Suppressing local particle oscillations in the Hamiltonian particle method for elasticity, *Int. J. Num. Meth. Eng.,* **81,** 1514–1528.

Levander, A.R., 1988. Fourth-order finite-difference P-SV seismograms, *Geophysics,* **53,** 1425–1436.

Madariaga, R., 1976. Dynamics of an expanding circular fault, *Bull. seism. Soc. Am.,* **65,** 163–182.

Marfurt, K.J., 1984. Accuracy of finite-difference and finite-element modeling of the scalar and elastic wave equations, *Geophysics,* **49,** 533–549.

Mariotti, C., 2007. Lamb's problem with the lattice model Mka3D, *Geophys. J. Int.,* **171,** 857–864.

Mercerat, E.D., Vilotte, J.P. & Sanchez-Sesma, F.J., 2006. Triangular spectral element simulation of two-dimensional elastic wave propagation using unstructured triangular grids, *Geophys. J. Int.,* **166,** 679–698.

Mullen, R. & Belytschko, T., 1982. Dispersion analysis of finite element semidiscretizations of the two-dimensional wave equation, *Int. J. Num. Meth. Eng.,* **18,** 11–29.

O'Brien, G.S. & Bean, C.J., 2004. A 3D discrete numerical elastic lattice method for seismic wave propagation in heterogeneous media with topography, *Geophys. Res. Lett.,* **31,** L14608, doi:10.1029/2004GL020069.

O'Brien, G.S., Bean, C.J. & Tapamo, H., 2009. Dispersion analysis and computational efficiency of elastic lattice methods for seismic wave propagation, *Comput. Geosci.,* **35,** 1768–1775.

Suzuki, Y., Koshizuka, S. & Oka, Y., 2007. Hamiltonian moving-particle semi-implicit (HMPS) method for incompressible fluid flows, *Comput. Meth. Appl. Mech. Eng.,* **196,** 2876–2894.

Suzuki, Y. & Koshizuka, S., 2008. A Hamiltonian particle method for non-linear elastodynamics, *Int. J. Num. Meth. Eng.,* **74,** 1344–1373.

Toomey, A. & Bean, C.J., 2000. Numerical simulation of seismic waves using a discrete particle scheme, *Geophys. J. Int.,* **141,** 595–604.

Virieux, J., 1986. P-SV wave propagation in heterogeneous media: velocity-stress finite difference method, *Geophysics,* **51,** 889–901.